

Super-Eddington growth of black holes in the early universe: effects of disc radiation spectra

Eishun Takeo,¹★ Kohei Inayoshi,² Ken Ohsuga,³ Hiroyuki R. Takahashi⁴
and Shin Mineshige¹

¹Department of Astronomy, Graduate School of Science, Kyoto University, Kitashirakawa, Oiwakecho, Sakyo-ku, Kyoto 606-8502, Japan

²The Kavli Institute for Astronomy and Astrophysics, Peking University, 5 Yiheyuan Road, Haidian District, Beijing 100871, P. R. China

³Center for Computational Sciences, University of Tsukuba, 1-1-1 Tennodai, Tsukuba, Ibaraki 305-8577, Japan

⁴Faculty of Arts and Sciences, Department of Natural Sciences, Komazawa University, 1-23-1 Komazawa, Setagaya, Tokyo 154-8525, Japan

Accepted 2019 July 7. Received 2019 June 25; in original form 2019 January 14

ABSTRACT

We investigate the properties of accretion flows on to a black hole (BH) with a mass of M_{BH} embedded in an initially uniform gas cloud with a density of n_{∞} in order to study rapid growth of BHs in the early Universe. In previous work, the conditions required for super-Eddington accretion from outside the Bondi radius were studied by assuming that radiation produced at the vicinity of the central BH has a single power-law spectrum $\nu^{-\alpha}$ at $h\nu \geq 13.6 \text{ eV}$ ($\alpha \sim 1.5$). However, radiation spectra surely depend on the BH mass and accretion rate, and determine the efficiency of radiative feedback. Here, we perform two-dimensional multifrequency radiation hydrodynamical simulations taking into account more realistic radiation spectra associated with the properties of nuclear accretion discs. We find that the critical density of gas surrounding the BH, above which transitions to super-Eddington accretion occur, is alleviated for a wide range of masses of seed BHs ($10 \lesssim M_{\text{BH}}/M_{\odot} \lesssim 10^6$) because photoionization for accretion disc spectra are less efficient than those for single power-law spectra with $1 \lesssim \alpha \lesssim 3$. For disc spectra, the transition to super-Eddington is more likely to occur for lower BH masses because the radiation spectra become too hard to ionize the gas. Even when accretion flows are exposed to anisotropic radiation, the effect due to radiation spectra shrinks the ionized region and likely leads to the transition to a wholly neutral accretion phase. Finally, by generalizing our simulation results, we construct a new analytical criterion required for super-Eddington accretion; $(M_{\text{BH}}/10^5 M_{\odot})(n_{\infty}/10^4 \text{ cm}^{-3}) \gtrsim 2.4(\langle \epsilon \rangle/100 \text{ eV})^{-5/9}$, where $\langle \epsilon \rangle$ is the mean energy of ionizing radiation from the central BH.

Key words: accretion, accretion discs – black hole physics – quasars: supermassive black holes – cosmology: theory.

1 INTRODUCTION

Observations of bright quasars led by accreting supermassive black holes (SMBHs) with masses of $\gtrsim 10^9 M_{\odot}$ at high redshift $z \gtrsim 6$ (or $\lesssim 1$ Gyr from the Big Bang) require rapid growth of black holes (BHs) in the early Universe (e.g. Fan et al. 2004; Mortlock et al. 2011; Wu et al. 2015; Bañados et al. 2018). SMBHs are expected to play crucial roles in the history of the Universe such as via co-evolution with their host galaxies (e.g. Silk & Rees 1998; King 2003; Murray, Quataert & Thompson 2005; Kormendy & Ho 2013), but their formation processes are still unclear.

A possible origin of high- z SMBHs is highly accreting stellar-mass BH seeds with $\sim 100 M_{\odot}$ (e.g. Haiman & Loeb 2001; Madau & Rees 2001; Volonteri, Haardt & Madau 2003; Li et al. 2007; Alvarez, Wise & Abel 2009; Alexander & Natarajan 2014a), which are remnants of massive Population III stars (Pop III) (e.g. Yoshida, Omukai & Hernquist 2008; Hosokawa et al. 2011; Stacy, Greif & Bromm 2012; Hirano et al. 2014; Hosokawa et al. 2016). Accreting gas forms an accretion disc which radiates with a luminosity of $L = \eta \dot{M} c^2$, where η is the radiation efficiency, \dot{M} is the accretion rate, and c is the speed of light. For a rapidly accreting BH, the radiation luminosity would exceed the Eddington value L_{Edd} , above which the radiation force due to electron scattering overcomes the BH gravity. Thus, the accretion rate could be limited at $\dot{M} \leq L_{\text{Edd}}/(\eta c^2)$. As a result of this, the BH growth time-scale from light seeds becomes significantly longer than the age of the

★ E-mail: takeo@kusastro.kyoto-u.ac.jp

Universe when high- z SMBHs already exist ($\gtrsim 1$ Gyr) in cases with $\eta \sim 0.1$ (Soltan 1982; Yu & Tremaine 2002). Thus, rapid growth of BHs via super-Eddington gas accretion is an attractive pathway to high- z SMBHs.

Another possibility is more massive BH seeds with $\sim 10^3$ – $10^5 M_\odot$ formed by direct collapse of supermassive stars in protogalaxies (e.g. Loeb & Rasio 1994; Oh & Haiman 2002; Bromm & Loeb 2003; Begelman, Volonteri & Rees 2006; Regan & Haehnelt 2009a, b; Hosokawa, Omukai & Yorke 2012; Hosokawa et al. 2013; Inayoshi, Omukai & Tasker 2014; Visbal, Haiman & Bryan 2014; Inayoshi & Tanaka 2015; Inayoshi, Visbal & Kashiyama 2015; Chon et al. 2016; Regan, Johansson & Wise 2016a, b; Hirano et al. 2017; Inayoshi, Li & Haiman 2018) and runaway stellar collisions (e.g. Omukai, Schneider & Haiman 2008; Devecchi & Volonteri 2009; Katz, Sijacki & Haehnelt 2015; Yajima & Khochfar 2016; Sakurai et al. 2017; Stone, Küpper & Ostriker 2017; Reinoso et al. 2018). Even for such heavy seeds, we need to require a high duty cycle of BH growth at the Eddington accretion rate.

The possibility of super-Eddington accretion has been explored by many authors. In fact, some of ultra-luminous X-ray sources are considered to be stellar-mass BHs accreting at super-Eddington rates (Fabbiano, Gioia & Trinchieri 1989; King et al. 2001; Watarai, Mizuno & Mineshige 2001), and narrow-line Seyfert-1 galaxies are presumably super-Eddington accretors (e.g. Wang et al. 1999; Mineshige et al. 2000). By means of two-dimensional radiation hydrodynamical simulation, Ohsuga et al. (2005) have revealed that supercritical accretion is realized as long as sufficient gas is supplied at the vicinity of the central BH. Ohsuga & Mineshige (2007) have concluded that trapping of diffusive photons in the optically thick accretion disc and anisotropic radiation are crucial to realize super-Eddington accretion (see also Begelman 1979; Ohsuga et al. 2009; Ohsuga & Mineshige 2011; Jiang, Stone & Davis 2014; Sądowski et al. 2015; Takahashi et al. 2016; Kitaki et al. 2018). On the other hand, gas supply from larger scale can be significantly suppressed due to photoionization heating and radiation momentum (e.g. Ciotti & Ostriker 2001; Alvarez et al. 2009; Ciotti, Ostriker & Proga 2009; Milosavljević, Couch & Bromm 2009a; Milosavljević et al. 2009b; Park & Ricotti 2011, 2012). Since the connection between BH feeding and feedback has been understood poorly yet, previous works with semi-analytical models adopted various prescriptions for BH accretion rates in the assembly history of dark matter haloes (e.g. Volonteri & Rees 2005; Tanaka & Haiman 2009; Alexander & Natarajan 2014b; Madau, Haardt & Dotti 2014; Pacucci & Ferrara 2015; Pezzulli, Valiante & Schneider 2016; Valiante et al. 2016; Pezzulli et al. 2017; Valiante et al. 2018).

Recently, Inayoshi, Haiman & Ostriker (2016) found the conditions for supercritical accretion in a spherically symmetric system exposed to intense radiation from the BH with $L \simeq L_{\text{Edd}}$. When the size of an ionized region r_{HII} surrounding the accreting BH is smaller than the Bondi radius r_B , the ionized region collapses due to intense inflows of neutral gas and thus the accretion system transits to an isothermal (≈ 8000 K) Bondi accretion solution with a high accretion rate of $\gtrsim 5000 L_{\text{Edd}}/c^2$. The transition criterion is written as

$$M_{\text{BH}} \times n_\infty \gtrsim 10^9 M_\odot \text{cm}^{-3} (T_\infty/10^4 \text{K})^{3/2}, \quad (1)$$

where n_∞ and T_∞ are density and temperature of the ambient gas. Even with super-Eddington radiation feedback ($L > L_{\text{Edd}}$), the above criterion does not change significantly (Sakurai, Inayoshi & Haiman 2016). Moreover, the criterion for supercritical accretion is allevi-

ated under anisotropic radiation fields (Sugimura et al. 2017; Takeo et al. 2018). We note that the transition criterion is characterized by a quantity of $M_{\text{BH}} \times n_\infty$ because $r_{\text{HII}}/r_B \propto (M_{\text{BH}} \times n_\infty)^{-2/3}$. Here r_{HII} is estimated by the Strömngren radius

$$r_{\text{Strm}} \equiv \left(\frac{3\dot{N}_{\text{ion}}}{4\pi n_{\text{HII}}^2 \alpha_B} \right)^{1/3}, \quad (2)$$

where \dot{N}_{ion} is the emission rate of ionizing photons, n_{HII} is the number density of ionized gas, and α_B is the case B radiative recombination rate.

The previous work assumed that radiation from the central region has a single power-law (hereafter PL) spectrum with $L_\nu \propto \nu^{-\alpha}$, where the spectral index α is often set to 1.5¹ (see also Section 4). However, the shape of the disc radiation spectrum would be more complicated. According to the analytic solutions of accretion discs, the disc surface temperature is described as $T_{\text{eff}}(R) \propto R^{-p}$ (e.g. Mineshige et al. 1994; Kato, Fukue & Mineshige 2008), where R is the distance from the central BH. Assuming the disc surface locally emits blackbody radiation with $T_{\text{eff}}(R)$, the spectrum is written as $L_\nu \propto \nu^{3-(2/p)}$; $L_\nu \propto \nu^{1/3}$ ($p = 3/4$) in the standard disc case (Shakura & Sunyaev 1973), and $L_\nu \propto \nu^{-1}$ ($p = 1/2$) in the slim disc case (Abramowicz et al. 1988) (see Section 2.3 for more details). Moreover, since the disc temperature reaches $\sim 10^7$ K, the maximum energy of the continuum spectrum is as high as ~ 1 keV (e.g. Watarai 2006), which is much higher than the mean photon energy of the PL spectrum ≈ 40.8 eV. This fact implies that radiative feedback effects for disc spectra are less efficient than that for the PL spectrum because the cross-section to bound-free absorption of hydrogen atoms is $\sigma_{\text{bf,H}} \propto \nu^{-3}$ (e.g. Draine 2011). On the other hand, electrons primarily produced by X-ray ionization are energetic enough to ionize the ambient gas (e.g. Shull 1979; Shull & van Steenberg 1985; Ricotti, Gnedin & Shull 2002).

In this paper, we investigate the conditions for super-Eddington accretion under radiation with disc spectra associated with the standard and slim accretion disc model. We performed two-dimensional hydrodynamical simulations, including one-dimensional multifrequency radiation transfer and primordial chemical reaction networks. We first conduct simulations under isotropic radiation from the central accretion disc. We construct an analytical formula for the criterion required for super-Eddington accretion under isotropic radiation and show that the conditions are alleviated for a wide range of BH masses, compared to the cases with single PL spectra. Next, we perform simulations of accretion flows exposed to anisotropic radiation and investigate effects of the disc spectrum on to the inflow rate and conditions for the transition to a wholly neutral accretion phase.

The rest of this paper is organized as follows: in Section 2, we describe the methodology of our numerical simulations. In Section 3, we show our simulation results and give the conditions required for super-Eddington accretion. In Section 4, we discuss the analytical formula for the transition, the stability of highly accreting system after the transition, and caveats of our simulation set-ups. In Section 5, we summarize the conclusion of this paper.

¹Observed and calculated radiation spectra at $13.6 \lesssim h\nu/\text{eV} \lesssim 2$ keV are fit by power law with $\alpha \sim 1.1$ – 1.5 (Liu, Mineshige & Ohsuga 2003, and references therein).

2 METHODS

Our goal is to study conditions for super-Eddington accretion led by gas supply from larger scales. Gas accretion begins from a critical radius, the so-called Bondi radius, defined by

$$r_B \equiv \frac{GM_{\text{BH}}}{c_\infty^2} \simeq 1.97 \times 10^{14} m_{\text{BH}} T_{\infty,4}^{-1} \text{ cm}, \quad (3)$$

and the Bondi accretion rate for isothermal gas is given by

$$\dot{M}_B \equiv \pi e^{3/2} \rho_\infty \frac{G^2 M_{\text{BH}}^2}{c_\infty^3}, \quad (4)$$

where $m_{\text{BH}} \equiv M_{\text{BH}}/M_\odot$, $T_{\infty,4} \equiv (T_\infty/10^4 \text{ K})$, $c_\infty \equiv \sqrt{\gamma \mathcal{R} T_\infty / \bar{\mu}}$ is the sound speed, γ is the specific heat ratio, \mathcal{R} is the gas constant, and $\bar{\mu}$ is the mean molecular weight. Note that the Bondi radius and rate as reference values are calculated by setting $\gamma = 1$, $\bar{\mu} = 1.23$, and $T_\infty = 10^4 \text{ K}$.

2.1 The code

We perform two-dimensional hydrodynamical simulations of axisymmetric flows with one-dimensional radiation transfer and chemical reaction networks (Takeo et al. 2018). Here we adopt the hydrodynamical simulation code developed in Takahashi & Ohsuga (2013). The advection terms for the ideal fluid are computed using the Harten–Lax–vanLeer Riemann solver (Harten, Lax & van Leer 1983), and the second-order accuracy in space and time are ensured (van Leer 1977). We adopt the spherical coordinates of (r, θ, ϕ) with the polar axis ($\theta = 0$ and π) perpendicular to the disc plane. We add the radiation and chemical codes taken from Inayoshi et al. (2016) with necessary modifications.

2.2 Basic equations

The basic equations of the hydrodynamical part are the equation of continuity

$$\frac{\partial \rho}{\partial t} + \nabla \cdot (\rho \mathbf{v}) = 0, \quad (5)$$

the equations of motion

$$\frac{\partial (\rho v_r)}{\partial t} + \nabla \cdot (\rho v_r \mathbf{v}) = -\frac{\partial p}{\partial r} + \rho \left(\frac{v_\theta^2}{r} + \frac{v_\phi^2}{r} \right) - \rho \frac{\partial \psi}{\partial r} + f_{\text{rad}}, \quad (6)$$

$$\frac{\partial (\rho r v_\theta)}{\partial t} + \nabla \cdot (\rho r v_\theta \mathbf{v}) = -\frac{\partial p}{\partial \theta} + \rho v_\phi^2 \cot \theta, \quad (7)$$

$$\frac{\partial (\rho r v_\phi \sin \theta)}{\partial t} + \nabla \cdot (\rho r v_\phi \sin \theta \mathbf{v}) = 0, \quad (8)$$

and the energy equation

$$\frac{\partial e}{\partial t} + \nabla \cdot [(e + p)\mathbf{v}] = -\frac{GM_{\text{BH}}\rho}{r^2} v_r - \Lambda + \Gamma. \quad (9)$$

where ρ is the gas density, $\mathbf{v} = (v_r, v_\theta, v_\phi)$ is the velocity, p is the gas pressure, and f_{rad} is the radiation force. We consider the gravity of the central BH ($r = 0$) and neglect the gas self-gravity. Since the general relativistic effect is negligible, the gravitational potential is given by $\psi = -GM_{\text{BH}}/r$. The total energy per volume is defined as $e \equiv e_{\text{int}} + \rho |\mathbf{v}|^2/2$, e_{int} is the gas internal energy density, Λ is

the cooling rate per volume, and Γ is the radiative heating rate. We assume the equation of state of ideal gas as $p = (\gamma - 1)e_{\text{int}}$ for $\gamma = 5/3$.

We solve the multifrequency radiative transfer equation

$$\frac{1}{r^2} \frac{d}{dr} (r^2 F_v) = -\rho \kappa_v c E_v, \quad (10)$$

where F_v is the radiation flux, E_v is the radiation energy density, and κ_v is the absorption opacity. The radiation field is assumed to be steady because the light crossing time is much shorter than the hydrodynamical time-scale. The frequency range is set to $h\nu_{\text{min}} (= 13.6 \text{ eV}) \leq h\nu \leq h\nu_{\text{max}} (= 100 \text{ keV})$, where h is the Planck constant. We note that only the radial component of the radiation flux is calculated because non-radial components produced by radiative recombination is negligible (see Section 4 in Takeo et al. 2018). Since the ionized gas is optically thin to electron scattering, we assume $F_v = cE_v$ on the right-hand-side of equation (10).

We consider cooling processes associated with H, He, He⁺ atoms and free–free emission (Glover & Jappsen 2007), assuming the optically thin cooling rates. In order to estimate their rates, we solve chemical reaction networks including six species of H, H⁺, He, He⁺, He⁺⁺, and e⁻. The abundance of He nuclei relative to H nuclei is set to 8.33×10^{-2} . Here we consider photoionization, collisional ionization, and radiative recombination (Abel et al. 1997; Glover & Jappsen 2007), including effects of the secondary ionization (see below). Photoionization due to diffusive recombination photons is neglected, i.e. the case B recombination rate is adopted instead of the case A rate. The cooling/heating term in the energy equation (equation 9), the chemical reaction, and the radiative transfer equation (equation 10) are updated with an implicit method in order to solve them stably and save computation time. We set the time steps by setting the Courant number to 0.4.

The ionization rate coefficients and photoionization heating rates are calculated with the photon-conserving method (Whalen & Norman 2006). The primary ionization rates $k_{\text{ph},i}^p$ ($i = \text{H, He, and He}^+$) are estimated as

$$k_{\text{ph},i}^p = \int_{\nu_{\text{min}}}^{\nu_{\text{max}}} d\nu \frac{F_\nu}{h\nu} \sigma_{\text{bf},i}, \quad (11)$$

where $\sigma_{\text{bf},i}$ is the bound-free cross-section. Since the energy of electrons produced by primary ionization is higher than the ionization potential energy, the electrons further ionize neutral hydrogen nearby (e.g. Shull 1979; Shull & van Steenberg 1985). The secondary ionization rates for species $j = \text{H, and He}$ are

$$k_{\text{ph},j}^s = \sum_{i=\text{H,He}} \int_{\nu_{\text{min}}}^{\nu_{\text{max}}} d\nu \frac{F_\nu}{h\nu} \sigma_{\text{bf},j} \Phi^j(E_i, x_{\text{H}^+}) \frac{x_i}{x_j}, \quad (12)$$

where x_j is the abundance of species j , $\Phi^j(E_i, x_{\text{H}^+})$ is the fraction of secondary ionization of species j per primary electron of energy $E_i \equiv h\nu - I_i$, and I_i is the ground-state ionization potential energy of the species i . The total photoionization rate is given by the sum of primary and secondary ionization rates. The photoionization heating rate ($i = \text{H, He, and He}^+$) is

$$\Gamma_i = \int_{\nu_{\text{min}}}^{\nu_{\text{max}}} d\nu \frac{F_\nu}{h\nu} \sigma_{\text{bf},i} E_h(E_i, x_{\text{H}^+}), \quad (13)$$

E_h is the energy of primary electrons deposited as heat. We adopt the functional forms of Φ^{H} , Φ^{He} , and E_h (Ricotti et al. 2002). Note that secondary ionization of He⁺ is negligible (Shull & van Steenberg 1985). The radiation force caused by electron scattering and bound-

free absorption is given by

$$f_{\text{rad}} = \frac{nX_e}{c} \int_{\nu_{\text{min}}}^{\nu_{\text{max}}} \sigma_{\text{es}} F_{\nu} d\nu + \frac{\Gamma^{\text{P}}}{c}, \quad (14)$$

where Γ^{P} is the sum of the heating rates due to primary ionization of H, He, and He^+ atoms.

2.3 Disc radiation models

In order to study the effect of radiation produced from the nuclear accretion disc, we adopt models for the radiation spectra. Since the accretion rate through the disc we consider is as high as $\dot{m} \equiv \dot{M}/\dot{M}_{\text{Edd}} \gtrsim 10^{-2}$, where $\dot{M}_{\text{Edd}} \equiv L_{\text{Edd}}/c^2$ and L_{Edd} is the Eddington luminosity, the disc emission can be approximated as multicolour blackbody spectra (e.g. Kato et al. 2008). The specific radiation luminosity is calculated as

$$L_{\nu} = 2 \int_{R_{\text{in}}}^{R_{\text{out}}} dR 2\pi R B_{\nu}[T_{\text{eff}}(R)], \quad (15)$$

where $B_{\nu}(T_{\text{eff}})$ is the blackbody intensity with an effective temperature of T_{eff} , and $R_{\text{in(out)}}$ is the inner (outer) radius of the disc (R is the radius of the cylindrical coordinate). The disc outer radius is set to $R_{\text{out}} = 10^4 r_{\text{Sch}}$ as our fiducial value, where $r_{\text{Sch}} \equiv 2GM_{\text{BH}}/c^2$ is the Schwarzschild radius. Note that we discuss the dependence of our results on the choice of R_{out} in Section 4. For $\dot{m} < 10$, we set the inner disc radius to the innermost stable circular orbit (ISCO) for a non-spinning BH ($R_{\text{in}} = 3 r_{\text{Sch}}$). In the slim disc cases with $\dot{m} > 40$, we set $R_{\text{in}} = 1.1 r_{\text{Sch}}$ because the gas is optically thick even inside the ISCO. For $10 \leq \dot{m} \leq 40$, we estimate R_{in} with a linear interpolation in the plane of $\log \dot{m} - \log R_{\text{in}}$. The radial structure of the effective temperature is given by Watarai (2006) as

$$T_{\text{eff}}(R) = 2.5 \times 10^7 \text{ K } f^{1/8} \left(\frac{m_{\text{BH}}}{10}\right)^{-1/4} \left(\frac{R}{r_{\text{Sch}}}\right)^{-1/2} \mathcal{F}(R, \dot{m}), \quad (16)$$

where

$$\mathcal{F}(R, \dot{m}) \equiv \begin{cases} (1 - \sqrt{3r_{\text{Sch}}/R})^{1/4} & \text{for } \dot{m} \leq 10, \\ (1 - \sqrt{R_{\text{in}}/R})^{1/4} & \text{for } 10 < \dot{m} < 40, \\ 1 & \text{for } \dot{m} \geq 40, \end{cases} \quad (17)$$

and f is a function of R and \dot{m} which connects the standard and slim disc solution smoothly.² When the accretion rate is sufficiently high ($\dot{m} \gg 1$), the advection cooling time-scale is shorter than the photon diffusion time-scale within a characteristic radius, so-called the photon-trapping radius $R_{\text{tr}} \equiv \dot{m} r_{\text{Sch}}$, where $f \simeq 1$ and $\mathcal{F} \simeq 1$. At $R \gtrsim R_{\text{tr}}$, optically thick radiative cooling in the disc is dominant and $f \propto R^{-2}$. Thus, most of the radiation is produced within the

trapping radius, and the bolometric luminosity is expressed as

$$\frac{L}{L_{\text{Edd}}} = 2 \left[1 + \ln \left(\frac{\dot{m}}{20} \right) \right], \quad (19)$$

for $\dot{m} > 20$ (Watarai et al. 2000). We also model the angular dependence of radiation fields in the same way as in Takeo et al. (2018),

$$F_{\nu}(r = r_{\text{min}}, \theta) = \frac{(\mathcal{N} + 1)L_{\nu}}{4\pi r_{\text{min}}^2} \cos^{\mathcal{N}} \theta, \quad (20)$$

where r_{min} is the size of the innermost grid (see Section 2.5) and \mathcal{N} characterizes the anisotropy of radiation fields. In this study, we explore both isotropic cases ($\mathcal{N} = 0$) and anisotropic cases ($\mathcal{N} = 4$).

Furthermore, we consider the photon redshift effect, i.e. the radiation intensity observed at infinity $I_{\nu_{\text{obs}}}$ is connected with the intensity $I_{\nu_{\text{em}}}$ at the photon-emitting point ($R = R_{\text{em}}$) on the disc surface as $I_{\nu_{\text{obs}}} = (\nu_{\text{obs}}/\nu_{\text{em}})^3 I_{\nu_{\text{em}}}$, where we assume $\nu_{\text{obs}}/\nu_{\text{em}} = (1 - r_{\text{Sch}}/R)^{1/2}$ for simplicity.³

2.4 Emergent spectra from the disc

In the top panel of Fig. 1, we show the spectral shape of radiation from an accretion disc around the central BH with $m_{\text{BH}} = 10$ at an accretion rate of $\dot{m} = 1$ (blue) and $\dot{m} = 10^3$ (red). For the standard disc case ($\dot{m} = 1$), the spectrum is expressed by a multicolour blackbody spectrum of

$$L_{\nu}^{\text{D,st}} = 5.7 \times 10^{13} m_{\text{BH}}^{4/3} \dot{m}^{2/3} \nu^{1/3} \text{ erg s}^{-1} \text{ Hz}^{-1} \quad (21)$$

at the frequency range of $\nu_{\text{out}} \lesssim \nu \lesssim \nu_{\text{peak}}$, where

$$\nu_{\text{out}} \equiv 3.16 \times 10^{18} m_{\text{BH}}^{-1/4} \dot{m}^{1/4} \left(\frac{R_{\text{out}}}{r_{\text{Sch}}}\right)^{-3/4} \text{ Hz} \quad (22)$$

is the frequency of photons emitted from $R = R_{\text{out}}$ and

$$\nu_{\text{peak}} \equiv 1.01 \times 10^{17} m_{\text{BH}}^{-1/4} \dot{m}^{1/4} \text{ Hz} \quad (23)$$

is the peak frequency of the spectrum. The spectral shape is expressed by the Rayleigh–Jeans slope ($L_{\nu} \propto \nu^2$) at $\nu < \nu_{\text{out}}$, and has an exponential cut-off, the so-called Wien cut-off, at $\nu > \nu_{\text{peak}}$.

For the slim disc case ($\dot{m} = 10^3$), the disc spectrum has an additional component associated with the modification of the effective temperature as described in equation (16),

$$L_{\nu}^{\text{D,slim}} = 5.15 \times 10^{38} m_{\text{BH}} \nu^{-1} \text{ erg s}^{-1} \text{ Hz}^{-1}, \quad (24)$$

at the frequency range of $\nu_{\text{tr}} < \nu < \nu_{\text{peak}}$, where

$$\nu_{\text{tr}} \equiv 10^{17} (m_{\text{BH}}/10)^{-1/4} (\dot{m}/10^3)^{-1/2} \text{ Hz} \quad (25)$$

corresponds to the frequency of photons emitted from R_{tr} .

In the bottom panel of Fig. 1, we compare three different radiation spectra: a single PL with an index of $\alpha = 1.5$ (black), and disc spectra with $M_{\text{BH}} = 10$ (red), and $10^5 M_{\odot}$ (blue) for $\dot{m} = 10^3$. The disc spectrum with $m_{\text{BH}} = 10$ is harder than the PL spectrum: in fact, the difference of the luminosities at $h\nu = 13.6 \text{ Hz}$ is the order of

²The function f is defined as a ratio of the advection cooling rate to the viscous heating rate at radius R and satisfies

$$f = 0.5 \left(D^2 X^2 + 2 - DX \sqrt{D^2 X^2 + 4} \right), \quad (18)$$

where $X \equiv R/(\dot{m} r_{\text{Sch}})$, and we set $D = 2.81$.

³Although general relativistic (GR) effects on accretion discs are studied recently (e.g. Sądowski et al. 2015; Takahashi et al. 2016; Narayan, Sądowski & Soria 2017), we do not adopt the details of their findings in our disc model. In fact, GR effects would not be so important for super-Eddington accretion discs because the photosphere $r_{\text{ph}} \sim \dot{m} r_{\text{g}}$ becomes much larger than the Schwarzschild radius (e.g. Kitaki et al. 2017).

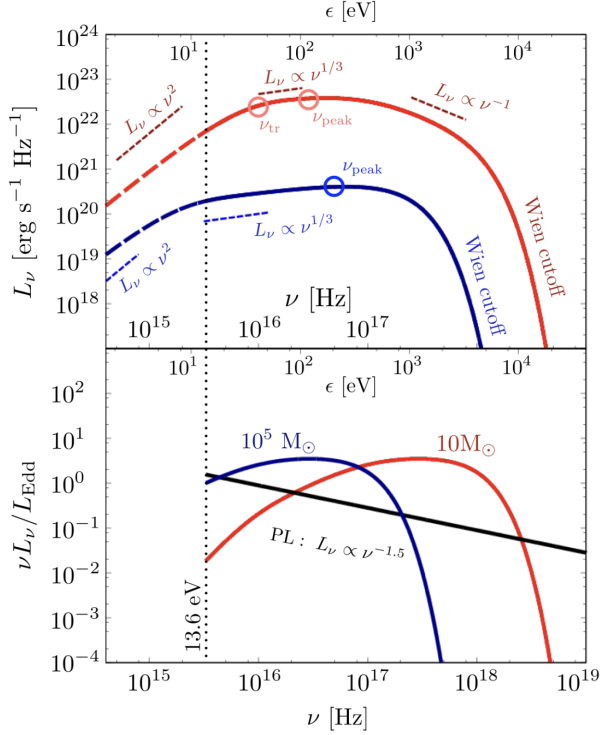


Figure 1. Spectral models for radiation emitted from the nuclear BH accretion disc. In the top panel, disc spectra with $m_{\text{BH}} = 10$ for $\dot{m} = 1$ (blue; the standard disc) and $\dot{m} = 10^3$ (red; the slim disc) are shown. Note that non-ionizing photons with lower energies of $h\nu < 13.6$ eV (dashed) are not taken into account. In the bottom panel, we present disc spectra with $\dot{m} = 10^3$ for $m_{\text{BH}} = 10$ (red) and $m_{\text{BH}} = 10^5$ (blue), and the PL spectrum $L_\nu \propto \nu^{-1.5}$ with $\dot{m} = 10^3$ (black).

$\sim 10^2$. The disc spectrum becomes softer as the BH mass increases following $T_{\text{eff}} \propto m_{\text{BH}}^{-1/4}$.

2.5 Initial and boundary conditions

We set a computational domain of $r_{\text{min}} \leq r \leq r_{\text{max}}$ and $0 \leq \theta \leq \pi$, where $(r_{\text{min}}, r_{\text{max}}) = (0.007 r_{\text{B}}, 6 r_{\text{B}})$ for isotropic radiation, and $(r_{\text{min}}, r_{\text{max}}) = (0.07 r_{\text{B}}, 60 r_{\text{B}})$ for anisotropic radiation. In the case with anisotropic radiation, we set a larger simulation box because the ionized region towards the bipolar directions tends to be larger than that in isotropic cases. We set logarithmically spaced grids in the radial direction and uniformly spaced grids in the polar direction. The number of the grid points is set to $(N_r, N_\theta) = (100, 120)$.

As our initial conditions, we set a neutral uniform and static ($\mathbf{v} = 0$) gas cloud with a density n_∞ and temperature $T_\infty = 10^4$ K. The BH mass is assumed to be constant throughout the simulations. Since our main goal is to derive the conditions for super-Eddington transitions, we explore a wide range of the ambient density and BH mass: $10^4 \leq n_\infty/\text{cm}^{-3} \leq 3 \times 10^9$ and $1 \leq M_{\text{BH}}/M_\odot \leq 10^5$. Our model set-up with isotropic radiation is summarized in Table 1. We impose the absorption inner-boundary conditions which damps the gas density, the velocity, and gas pressure smoothly (e.g. Kato, Mineshige & Shibata 2004), and the free outer-boundary conditions for three components of the velocity and the specific entropy. We also fix the same gas density at $r = r_{\text{max}}$ as the initial value for grids with an inflow velocity i.e. $v_r(r = r_{\text{max}}) < 0$, otherwise the free boundary condition is imposed for the density. The reflection

Table 1. Model parameters and results for isotropic radiation cases.

| Model | $M_{\text{BH}}(M_\odot)$ | $n_\infty(\text{cm}^{-3})$ | Transition | $t_{\text{tran, end}}(t_{\text{dyn}})$ |
|----------|--------------------------|----------------------------|------------|--|
| 1e0M18N0 | 1 | 1×10^8 | N | 5.2 |
| 1e0M38N0 | 1 | 3×10^8 | N | 5.2 |
| 1e0M58N0 | 1 | 5×10^8 | Y | 4.3 |
| 1e0M19N0 | 1 | 1×10^9 | Y | 1.8 |
| 1e0M39N0 | 1 | 3×10^9 | Y | 0.75 |
| 1e1M37N0 | 10 | 3×10^7 | N | 5.5 |
| 1e1M18N0 | 10 | 1×10^8 | Y | 2.9 |
| 1e2M36N0 | 10^2 | 3×10^6 | N | 5.6 |
| 1e2M17N0 | 10^2 | 1×10^7 | Y | 4.4 |
| 1e2M37N0 | 10^2 | 3×10^7 | Y | 1.6 |
| 1e5M14N0 | 10^5 | 1×10^4 | N | 6.8 |
| 1e5M34N0 | 10^5 | 3×10^4 | Y | 6.1 |
| 1e5M54N0 | 10^5 | 5×10^4 | Y | 2.7 |
| 1e5M15N0 | 10^5 | 1×10^5 | Y | 1.3 |

Note. Column (1) model ID, (2) BH mass, (3) ambient gas density, (4) symbols Y (N) denoting that the transition occurs (does not occur) within the simulation time, and (5) the time when the transition occurs t_{tran} (bold) and the duration t_{end} (thin, for models without transitions) in units of $t_{\text{dyn}} (\equiv r_{\text{B}}/c_\infty)$.

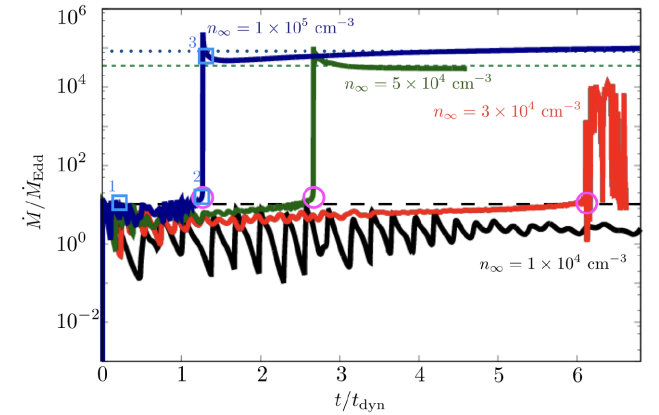


Figure 2. Time evolution of accretion rates on a BH with a mass of $M_{\text{BH}} = 10^5 M_\odot$ embedded in a gas cloud with different densities of $n_\infty = 10^4$ (black), 3×10^4 (red), 5×10^4 (green), and 10^5cm^{-3} (blue). For the lowest density ($n_\infty = 10^4 \text{cm}^{-3}$), the gas accretion occurs episodically due to photoionization and heating. For higher densities with $n_\infty > 3 \times 10^4 \text{cm}^{-3}$, the accretion rates behave similarly in the early stages where the rates are limited around $\dot{M} = 10 \dot{M}_{\text{Edd}}$ (black dashed), but transit into rapid accretion phases where the rates are approximated as the Bondi accretion rates for the given ambient densities (horizontal dotted lines). The transition epochs are marked by open circles. The open squares indicate the epochs at which we show the radial profiles in Fig. 3.

symmetry with respect to the polar axis is imposed for non-radial components of the velocity.

3 RESULTS

Fig. 2 presents the time evolution of accretion rates on a BH with $M_{\text{BH}} = 10^5 M_\odot$ for $n_\infty = 1 \times 10^4 \text{cm}^{-3}$ (black), $3 \times 10^4 \text{cm}^{-3}$ (red), $5 \times 10^4 \text{cm}^{-3}$ (green), and $1 \times 10^5 \text{cm}^{-3}$ (blue). The horizontal dashed line shows the Eddington accretion for a 10 percent of the radiation efficiency.

For the lowest density of $n_\infty = 1 \times 10^4 \text{cm}^{-3}$ (Model 1e5M14N0), the accretion rate behaves episodically due to radiative

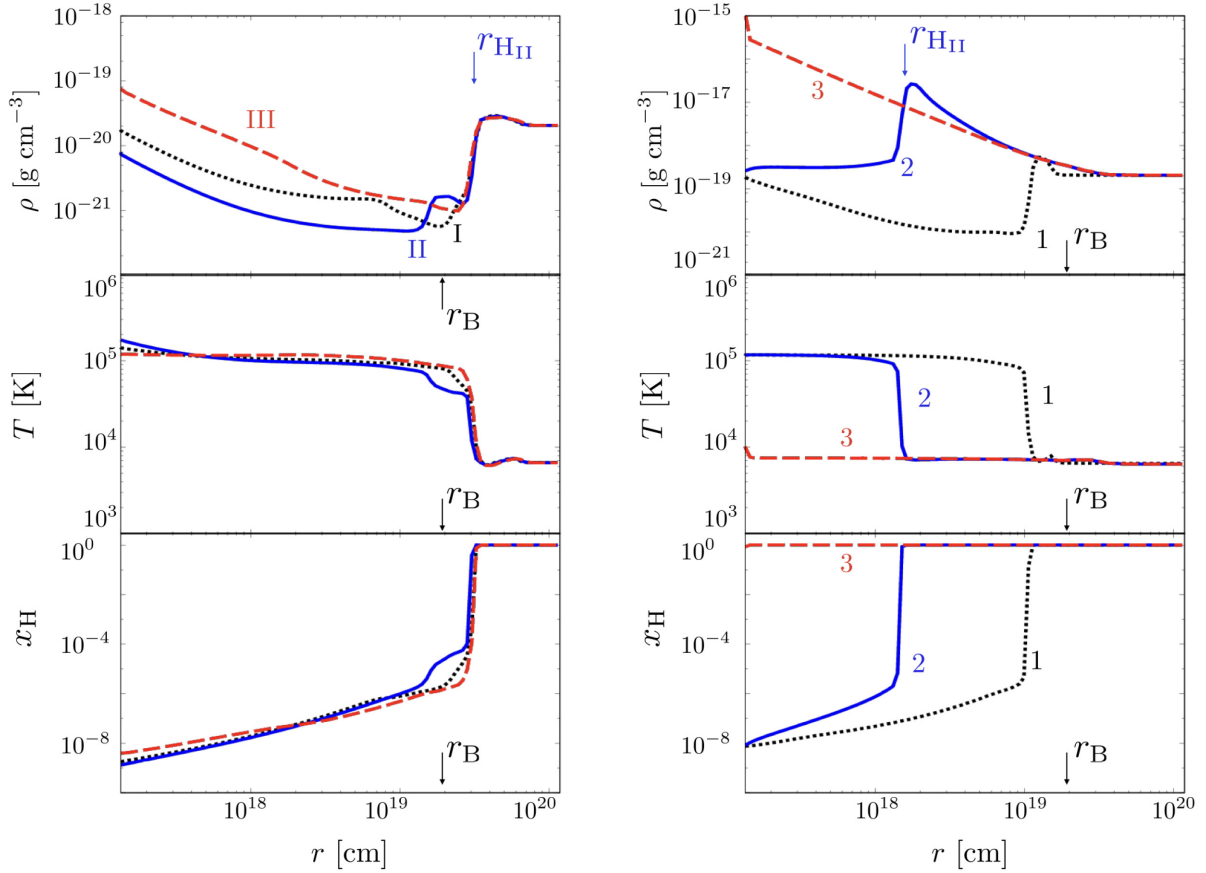


Figure 3. Radial structure of the gas density (top), temperature (middle), neutral fraction (bottom) at the equatorial plane. In the left-hand panels, we present the profiles for Model 1e5M14N0, where the accretion occurs episodically without a transition to super-Eddington phases, at three different epoch during an oscillation: $t/t_{\text{dyn}} = 1.46$ (dotted), 1.55 (solid), and 1.69 (dashed). In the right-hand panels, we show those for Model 1e5M15N0, where the accretion rate transitions to a super-Eddington value, at $t/t_{\text{dyn}} = 0.334$ (dotted), 1.25 (solid), and 1.38 (dashed). For the case without the transition, the location of the ionization front r_{HII} is outside the Bondi radius, while the ionized region is always confined inside the Bondi radius for the case with the transition.

heating (black curve in Fig. 2). The physical origin of the oscillation is explained in what follows. In Fig. 3 (left-hand panel), we present the radial structure of the gas density, temperature, and neutral fraction at different three epochs in an oscillation period. For this case, radiation associated with BH accretion propagates outwards, and the gas outside the Bondi radius is ionized and heated up ($r_{\text{HII}} > r_{\text{B}}$, see phase I). Inside the ionized region, ionized gas within a new sonic radius at $\simeq 0.1 r_{\text{B}}$ for the hot gas with $T \sim 10^5$ K can accrete on to the central region, while gas outside the radius flows outwards. As a result, a density cavity forms within the ionized region, where the outward and inward gas pressure forces are balanced. When the ionized gas is depleted from the ionized region, a density bump forms inside the ionization front because pressure inside decreases (phase II). This density bump provides a positive pressure gradient ($\partial p/\partial r > 0$) and accelerate gas accretion ($\dot{m} \approx 7.46$, phase III). This episodic behaviour has been studied in detail in previous studies (e.g. Ciotti & Ostriker 2001; Milosavljević et al. 2009a; Park & Ricotti 2011, 2012). The time-averaged accretion rate results in as small as $\langle \dot{M} \rangle \approx 1.6 \dot{M}_{\text{Edd}}$.

With the highest ambient density ($n_{\infty} = 10^5 \text{ cm}^{-3}$), the episodic accretion behaviour ceases unlike the lowest density case. Instead, the accretion rate has a big jump to a very high value (red, green, and blue curves in Fig. 2). The open circles indicate the epochs when transitions to super-Eddington accretion occur. In Fig. 3 (right-

hand panel), we present the radial structure of the gas density, temperature, and neutral fraction for the highest density (Model 1e5M15N0) at different three epochs of $t/t_{\text{dyn}} = 0.334$ (phase 1), 1.25 (phase 2), and 1.38 (phase 3). At the beginning, an ionized region forms and the gas is heated up to $T \sim 10^5$ K as in the lowest density case. However, because of the higher density, the size of the ionized region never becomes larger than the Bondi radius ($r_{\text{HII}} < r_{\text{B}}$). As a result of this, a dense shell forms at $r_{\text{HII}} \lesssim r \lesssim r_{\text{B}}$ and pushes the ionized gas inwards (phase 2). During the transition, the ionized region shrinks and disappears because of efficient radiative recombination (phase 3). The accretion rate jumps dramatically because the dense shell collapses and supplies a large amount of gas. Thus, the accretion flow settles down to an isothermal Bondi accretion solution with $T \approx 8000$ K (blue dotted line).

For the intermediate values at $10^4 \text{ cm}^{-3} < n_{\infty} < 10^5 \text{ cm}^{-3}$, the accretion rate begins to rise drastically at the transition epochs where a neutral shell infalls into the centre as shown in the previous case. However, the accretion rate oscillates in short-time durations without settling to steady states as shown by red curve because in the burst phases, radiation force slightly exceeds ram pressure of neutral gas inflows and a tiny ionized region forms transiently. As a result, the time-averaged accretion rate is as high as $\langle \dot{m} \rangle \simeq 2.9 \times 10^3$.

We note that this episodic behaviour seems a numerical artefact. As discussed in Section 4.2, if all the radiation from the nuclear accretion disc was injected at a radius much larger than the true

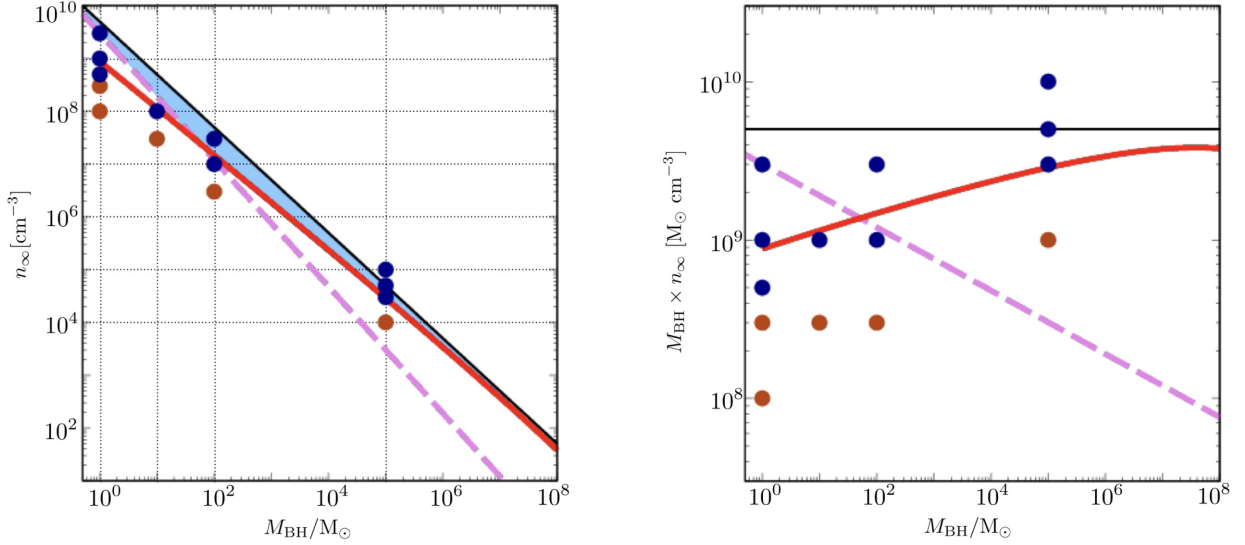


Figure 4. Summary of the results for different values of the BH mass M_{BH} and ambient gas density n_{∞} for isotropic radiation. Each circle symbol indicates whether the transition to super-Eddington accretion occurs (blue) or the accretion rate behaves episodically (orange). The transition criterion for disc spectra and a single PL spectrum ($L_{\nu} \propto \nu^{-1.5}$) are shown by red and black curves, respectively. The dashed line presents the stability conditions of rapid accretion after the transition, i.e. inward ram pressure of the inflow overcomes outward force caused by radiation with $L > L_{\text{Edd}}$ (see Section 4.2). The shaded region in the left-hand panel denotes the parameter space where the transition criterion is alleviated from that for the PL spectrum and the subsequent super-Eddington accretion is stable.

location of photosphere (i.e. $r_{\text{min}} > r_{\text{ph}}$), ram pressure of the inflow at the ionization front could be significantly underestimated and become weaker than radiation force. Furthermore, the luminosity of ionizing photons injected at r_{min} would be overestimated because the true spectrum after the transition would be softer than the slim-disc one. Thus, the two effects are expected to cease the numerical artefact. We demonstrate this for the case of $n_{\infty} = 5 \times 10^4 \text{ cm}^{-3}$ (green curve),⁴ by replacing the spectrum with a dilute blackbody spectrum with an effective temperature of $T_{\text{eff}} = (L/4\pi R_{\text{tr}}^2 \sigma_{\text{SB}})^{1/4}$, where σ_{SB} is the Stefan–Boltzmann constant, and $r_{\text{ph}} \approx R_{\text{tr}}$ is approximated. Note that this is a conservative treatment because the trapping radius is always located inside the photosphere, and the effective temperature measured with R_{tr} is higher than the true one. As a result, we find that a super-Eddington transition stably proceeds and the accretion flow approaches an isothermal Bondi profile.

In Fig. 4, we summarize our results for different values of M_{BH} and n_{∞} under isotropic radiation with spectra associated with accretion discs. Each circle symbol indicates whether the transition to super-Eddington accretion occurs (blue) or the accretion rate behaves episodically without the transition (orange). For the latter cases, we follow the simulations over $t > 5 t_{\text{dyn}}$, which is long enough to confirm the result. The red solid (black solid) line presents the transition criterion under the disc (single PL) spectrum (see Section 3.1 for derivation). The critical density for the transition n_{crit} is significantly reduced for lower BH masses with disc spectra. In fact, we find that $n_{\text{crit,D}}(M_{\text{BH}}) \simeq 0.1 n_{\text{crit,PL}}(M_{\text{BH}})$ for $M_{\text{BH}} \lesssim 10^2 M_{\odot}$, and $n_{\text{crit,D}}(M_{\text{BH}}) \simeq 0.6 n_{\text{crit,PL}}(M_{\text{BH}})$ for $M_{\text{BH}} \simeq 10^5 M_{\odot}$.

⁴Numerical simulations setting a smaller value of r_{min} require a long computational time until the accretion flow reaches the final steady state. Instead of this treatment, we decide to replace the radiation spectrum by a more realistic one with a lower mean photon energy.

3.1 Analytic arguments: the transition criterion

We here give a simple analytic argument for the conditions required for super-Eddington accretion, taking into account the radiation spectral effect. As discussed in Inayoshi et al. (2016), the transition conditions are well explained by the comparison of the Bondi radius and the size of the ionized region (see equations 2 and 3). For disc spectra, the number rate of ionizing photons absorbed by neutral hydrogen within the ionization front is estimated as

$$\dot{N}_{\text{ion,D}} \simeq \int_{\nu_{\text{min}}}^{\infty} d\nu \frac{L_{\nu}^{\text{D,st}}}{h\nu} \approx 1.22 \times 10^{46} m_{\text{BH}}^{5/4} \dot{m}^{3/4} \text{ s}^{-1}, \quad (26)$$

where $\dot{N}_{\text{ion,D}}$ is the ionizing photon number flux (in units of s^{-1}) and $L_{\nu}^{\text{D,st}}$ is the specific luminosity of radiation produced from a standard accretion disc because the BH accretion rate is sub-Eddington value ($\dot{m} \simeq 10$) before the transition. In the last expression, we neglect the contribution from ionizing photons with $\nu \geq \nu_{\text{peak}} = 10^{17} m_{\text{BH}}^{-1/4} \dot{m}^{1/4} \text{ Hz}$.⁵ Note that this approximation causes at most 20–40 per cent differences from the numerically integrated values for lower BH masses with $M_{\text{BH}} \lesssim 10^5 M_{\odot}$. Therefore, we obtain the ratio of the two radii

$$\begin{aligned} r_{\text{HII}}/r_{\text{B}} &\propto (\dot{N}_{\text{ion,D}})^{1/3} n_{\infty}^{-2/3} M_{\text{BH}}^{-1} \\ &\propto \left(M_{\text{BH}}^{7/8} \times n_{\infty} \right)^{-2/3}, \end{aligned} \quad (27)$$

which nicely agrees to the transition criterion shown in Fig. 4 (red). When the mean photon energy of the radiation spectrum is harder, the ionizing photon number flux becomes smaller for a given bolometric luminosity. Since the intrinsic radiation spectrum is harder for the lower BH mass, the photon absorption rate $\dot{N}_{\text{ion,D}}$ becomes lower, and the size of the ionized region becomes relatively

⁵Ionizing photons at frequencies of $\nu \gtrsim 10^{17} \text{ Hz}$ are hardly absorbed by neutral gas even outside the ionization front because of the steep frequency dependence of absorption cross-section of neutral hydrogen ($\sigma_{\text{H}} \propto \nu^{-3}$).

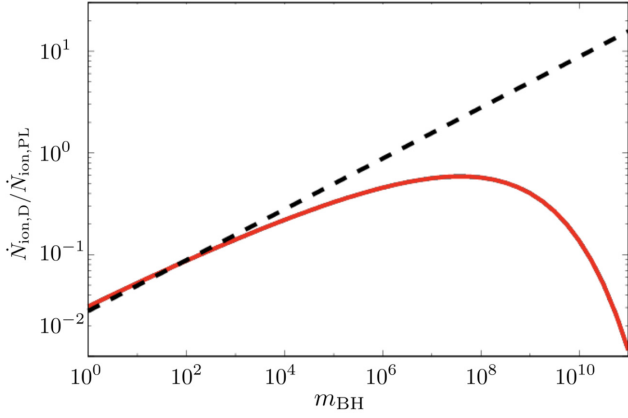


Figure 5. The ratio $\dot{N}_{\text{ion,D}}/\dot{N}_{\text{ion,PL}}$ as a function of m_{BH} where $\dot{m} = 10$ is set. The red solid curve (black dashed line) presents the value calculated numerically (analytically, see equation 29). For higher BH masses, the analytic formula (equation 29) is no longer valid because the peak frequency of the spectrum becomes comparable to the ionization threshold energy.

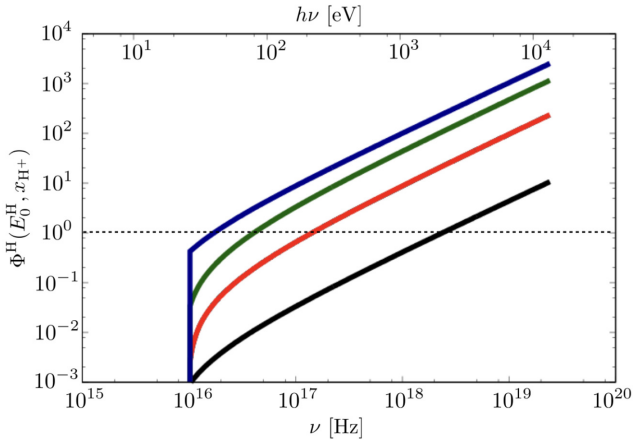


Figure 6. The fraction of secondary ionization of H atoms per primary electron of energy $E_{0,v}^i = h\nu - I^H$ with $x_{\text{H}^+} = 10^{-3}$ (blue), 10^{-1} (green), 0.4 (red), and 1.0 (black).

smaller. Therefore, the transition to super-Eddington accretion is more likely to occur.

It is worth comparing the transition criteria for disc spectra to those for PL spectra. Since the ionizing photon number flux for a PL spectrum with $\alpha = 1.5$ is estimated as

$$\dot{N}_{\text{ion,PL}} \approx 2.46 \times 10^{47} m_{\text{BH}} \dot{m} \text{ s}^{-1}, \quad (28)$$

where $L/L_{\text{Edd}} \simeq 0.1 \dot{m}$ at $\dot{m} \lesssim 20$, therefore we obtain the ratio of the two photon number fluxes

$$\frac{\dot{N}_{\text{ion,D}}}{\dot{N}_{\text{ion,PL}}} = 4.96 \times 10^{-2} m_{\text{BH}}^{1/4} \dot{m}^{-1/4}. \quad (29)$$

Note that the above scaling relation is valid for lower BH masses with $M_{\text{BH}} \lesssim 10^5 M_{\odot}$ (see black dashed in Fig. 5). Since the peak energy for higher BH masses becomes as low as the ionization threshold energy, the ionization photon number sharply drops for higher BH masses (see red curve Fig. 5), and thus the radiation feedback effect is significantly reduced.

We briefly mention the effects of secondary ionization on our results. In Fig. 6, we show the efficiency of secondary ionization of H atoms per electron produced by primary ionization with an

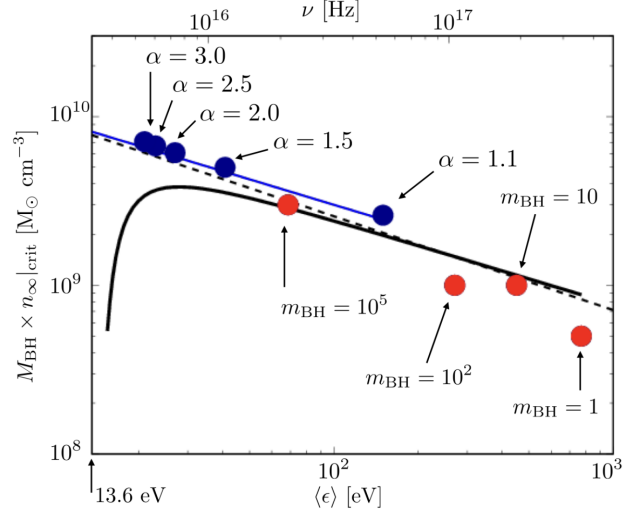


Figure 7. The critical value of $M_{\text{BH}} \times n_{\infty}$ for the transition as a function of the mean photon energy (ϵ) for different radiation spectra. The red circles show the numerical results for disc spectra with different BH masses. The critical value is well explained by the dashed line: $M_{\text{BH}} \times n_{\infty} \propto \langle \epsilon \rangle^{-5/9}$ in $70 \lesssim \langle \epsilon \rangle / \text{eV} \lesssim 800$. The blue circles represent the analytical results for PL spectra with different PL indexes of α , which are explained by the blue solid line: $M_{\text{BH}} \times n_{\infty} \propto \langle \epsilon \rangle^{-1/2}$.

energy of $E_{\text{H}} = h\nu - I_{\text{H}}$ for different electron fractions of $10^{-3} \leq x_{\text{H}^+} \leq 1.0$ (from the top to the bottom). The horizontal dashed line presents $\Phi^{\text{H}}(E_{\text{H}}, x_{\text{H}^+}) = 1$, above which secondary ionization becomes more effective than primary ionization. Since the photons causing primary ionization are at $\nu \lesssim 10^{17}$ Hz, the primary electrons hardly contribute to secondary ionization until the ionization degree increases to ~ 0.4 . As a result, secondary ionization can enhance the ionization degree near the ionization front, but does not expand the size of the ionization region.

4 DISCUSSION

4.1 Mean photon energy and transition criterion

As described in Section 3.1, the transition criterion for super-Eddington accretion depends on the shape of radiation spectra. Here, we generalize the criterion and rewrite the critical value of $M_{\text{BH}} \times n_{\infty}$ as a function of the mean photon energy. In Fig. 7, we summarize our simulation results for isotropic radiation. The red circles present the results for disc spectra for different BH masses of $M_{\text{BH}} = 1, 10, 10^2, \text{ and } 10^5 M_{\odot}$. By setting the accretion rate to $\dot{m} = 10$, we obtain the relation $\langle \epsilon \rangle = 7.7 \times 10^2 m_{\text{BH}}^{-0.23}$ eV. Thus, the transition criterion is expressed as

$$M_{\text{BH}} \times n_{\infty} \gtrsim 2.4 \times 10^9 M_{\odot} \text{ cm}^{-3} \left(\frac{\langle \epsilon \rangle}{100 \text{ eV}} \right)^{-5/9}. \quad (30)$$

Note that this equation is no longer valid for $\langle \epsilon \rangle \lesssim 70$ eV, and the critical value sharply drops at $\langle \epsilon \rangle \lesssim 20$ eV. In addition, blue circles present the critical values for PL spectra ($L_{\nu} \propto \nu^{-\alpha}$; $1.1 \leq \alpha \leq 3.0$), where the mean photon energy is $\langle \epsilon \rangle = h\nu_{\text{min}} \alpha / (\alpha - 1)$ for $\alpha > 1$, independent of both m_{BH} and \dot{m} (see also Park & Ricotti 2012). In the cases, the transition criterion is expressed as

$$M_{\text{BH}} \times n_{\infty} = 3.2 \times 10^9 M_{\odot} \text{ cm}^{-3} \left(\frac{\langle \epsilon \rangle}{100 \text{ eV}} \right)^{-1/2}, \quad (31)$$

Table 2. The photon number flux and mean photon energy affected by Comptonization.

| M_{BH}/M_{\odot} | $\dot{N}'_{\text{abs}}/\dot{N}_{\text{ion,D}}$ | $\langle \epsilon' \rangle/\text{eV}$ | $\langle \epsilon \rangle_{\text{D}}/\text{eV}$ |
|---------------------------|--|---------------------------------------|---|
| 10 | 8.4×10^{-2} | 2.0×10^3 | 4.0×10^2 |
| 10^2 | 8.8×10^{-2} | 1.6×10^3 | 2.4×10^2 |
| 10^3 | 9.3×10^{-2} | 1.2×10^3 | 1.5×10^2 |
| 10^4 | 0.11 | 7.2×10^2 | 94 |

Note. The number flux of ionizing photons absorbed by neutral hydrogen is calculated by $\dot{N}'_{\text{abs}} = \int_{\nu_{\text{min}}}^{\infty} d\nu L'_{\nu} (1 - e^{-\tau_{\nu}})/(h\nu)$, where the spectral shape of L'_{ν} is taken from the results of Kitaki et al. (2017), and the optical depth is estimated at the Bondi radius as $\tau_{\nu} = n_{\infty} r_{\text{B}} \sigma_{\text{H}}$. The mean photon energies of $\langle \epsilon' \rangle$ and $\langle \epsilon \rangle_{\text{D}}$ are estimated by taking the data from Kitaki et al. (2017) and by assuming the disc spectra, respectively. The accretion rate is set to $\dot{m} = 10^3$.

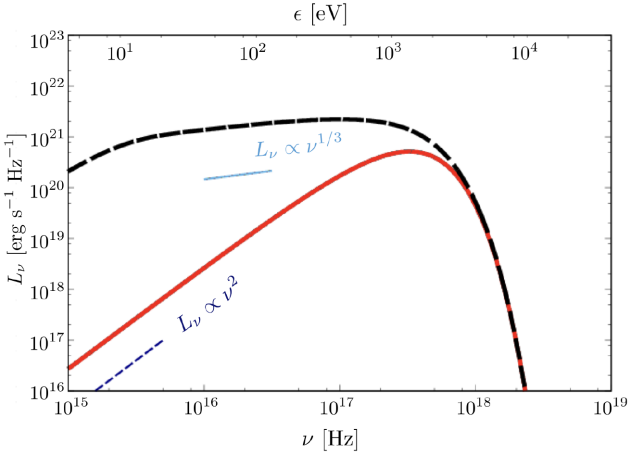


Figure 8. Dependence of radiation spectra on the choice of the disc outer edge: $R_{\text{out}} = 10 r_{\text{Sch}}$ (red solid) and $10^4 r_{\text{Sch}}$ (black dashed). We adopt $M_{\text{BH}} = 10 M_{\odot}$ and $\dot{m} = 10$.

which corresponds to the dashed line in Fig. 7. Note that the PL spectrum is normalized as $\eta \dot{m} L_{\text{Edd}} = \int_{\nu_{\text{min}}}^{\infty} d\nu L_{\nu}$, where $\eta = 0.1$.

Radiation spectra we observed in BH accreting systems are more complex than we considered in this paper. In some cases, radiation spectra consist of two components: thermal emission from the nuclear disc and non-thermal emission with PL spectra produced by Compton up-scattering in a hot corona (e.g. Haardt & Maraschi 1991; Svensson & Zdziarski 1994; Liu, Mineshige & Shibata 2002; Liu et al. 2003; Done & Kubota 2006). For super-Eddington accreting systems such as ULXs, a PL component is produced by a radiation-pressure-driven, hot ($\sim 10^{7.5} - 10^8$ K) outflow where soft photons from the accretion disc are hardened by both thermal and bulk Comptonization (e.g. Kawashima et al. 2009, 2012; Kitaki et al. 2017; Narayan et al. 2017). In the following, we discuss three effects changing the mean photon energy from disc spectra.

Recently, Kitaki et al. (2017) studied radiation spectra of super-Eddington accretion flows on to a BH with $10 \leq M_{\text{BH}}/M_{\odot} \leq 10^4$ under a mass inflow rate of $\dot{m} \simeq 10^3$ at $R = 10^3 r_{\text{Sch}}$. With Monte Carlo radiation transfer calculations, they found that a significant excess in the spectrum is produced at $h\nu \gtrsim$ a few \times keV due to Comptonization. In Table 2, we summarize the number flux of ionizing photons absorbed by neutral hydrogen and mean photon energy estimated by taking the data from Kitaki et al. (2017) (lower panels of their Fig. 5). Compared to the cases assuming disc spectra, the mean energies are boosted by a factor of 5–8. Since such

hard X-rays with $h\nu \gtrsim$ keV are hardly absorbed even by neutral hydrogen, the numbers of absorbed photons are reduced by one order of magnitude ($\dot{N}'_{\text{abs}}/\dot{N}_{\text{ion,D}} \simeq 0.1$). Therefore, the transition criterion is alleviated by a factor of ≈ 3 .

The size of the nuclear accretion disc would affect the feedback efficiency because ionizing photons with $13.6 \text{ eV} \lesssim h\nu \lesssim 1 \text{ keV}$ are produced from larger disc radii. In Fig. 8, we demonstrate the dependence of radiation spectra on the choice of the disc outer edge: $R_{\text{out}} = 10^4 r_{\text{Sch}}$ (black) and $10 r_{\text{Sch}}$ (red) for $M_{\text{BH}} = 10 M_{\odot}$ and $\dot{m} = 10$. For $R_{\text{out}} = 10 r_{\text{Sch}}$, the spectrum is no longer expressed as a multicolour blackbody spectrum but by the Rayleigh–Jeans law. Thus, the number flux of ionizing photons at $\nu \lesssim 3 \times 10^{17}$ Hz is significantly reduced and the mean photon energy increases to $\langle \epsilon \rangle \simeq 1.3 \text{ keV}$ from $\langle \epsilon \rangle \simeq 450 \text{ eV}$. As a result, the critical value for the transition would be reduced only by a factor of ≈ 2 . If R_{out} is much larger than the fiducial value, the emission rate of photons would increase only in the energy range with $h\nu < 13.6 \text{ eV}$. Since these photons are less energetic to ionize the ambient gas, the radiative feedback would not be enhanced, and the critical value for transitions would not be changed⁶.

In addition, the existence of dust grains in accretion flows significantly change the spectral shape due to UV attenuation caused by dust absorption and thus alleviate the criterion for super-Eddington accretion significantly. Recent work by Toyouchi et al. (2019) has found that rapid accretion of metal-polluted gas is allowed as long as $Z \lesssim 10^{-2} Z_{\odot}$, because ionizing radiation from the central BH is absorbed and re-emitted to infrared lights with lower energies ($h\nu \ll 13.6 \text{ eV}$).

4.2 Stability condition

We briefly discuss the stability of accretion flows at a very high inflow rate of $\dot{m} > 10^3$, exposed to intense radiation with a luminosity of $L > L_{\text{Edd}}$ (see also Sakurai et al. 2016). As shown in Fig. 3, during the transition a dense shell of neutral gas pushes the ionization front and a neutral region propagates inwards where a high accretion rate builds up. Thus, when the central BH is actually fed by the inflow and produces intense radiation, the accreting flow would already settle in an isothermal Bondi solution with $T \approx 8000$ K. However, the accretion flow cannot be neutral all the way down to the BH, but is ionized at a smaller radius r_{ph} where the flow becomes optically thick to continuum absorption. Considering H^- bound-free absorption opacity, we can estimate the location of the photosphere⁷ as

$$r_{\text{ph}} \simeq \left(\frac{3GM_{\text{BH}}\dot{M}_{\text{B}}}{8\pi\sigma_{\text{SB}}T_{\text{ph}}^4} \right)^{1/3} \simeq 7.1 \times 10^{13} \text{ cm} \left(\frac{\dot{m}}{10^4} \right)^{1/3} \left(\frac{m_{\text{BH}}}{10^4} \right)^{2/3}, \quad (32)$$

where the photospheric temperature is set to $T_{\text{ph}} = 2 \times 10^4$ K

⁶The choice of R_{out} depends on the angular momentum of inflowing gas from the Bondi radius. When the gas is optically thin to Ly α lines, a quasi-hydrostatic dense torus with a constant temperature of $T \simeq 8000$ K forms around the centrifugal radius of $r_{\text{cent}} (< r_{\text{B}})$. As long as the angular momentum is so small that $r_{\text{cent}} \lesssim 0.03 r_{\text{B}}$ is satisfied, the rate of accretion driven by viscosity can be comparable to the Bondi rate (Sugimura et al. 2018).

⁷In a partially ionized region, the strong dependence of opacity on gas temperature leads to a thermal-ionization instability (e.g. Meyer & Meyer-Hofmeister 1981; Kato et al. 2008). Though the location of the photosphere r_{ph} results is time-dependent, our order-of-magnitude estimate is not significantly changed.

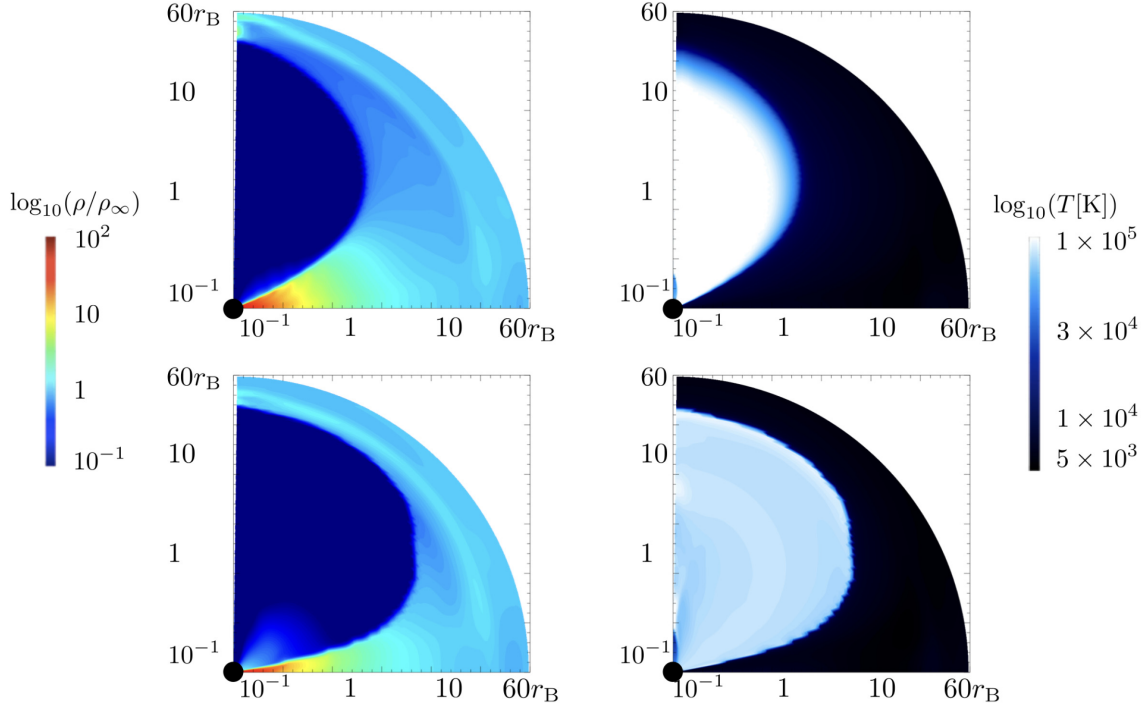


Figure 9. Two-dimensional distribution of the gas density (left-hand panels) and the temperature (right-hand panels) under the disc spectrum (top panels) and the PL spectrum (bottom panels) in cases with $1 M_{\odot}$, 10^9 cm^{-3} , and $\mathcal{N} = 4$. The elapsed time is $t = 1.7 \times 10^2 \text{ yr} = 20 t_{\text{dyn}}$.

(Inayoshi et al. 2016). Assuming that all incident radiation emitted from the photosphere is absorbed by the inflowing neutral gas and deposits momentum of L/c , the inflow velocity of neutral gas is accelerated to the free-fall value v_{ff} and push the gas at r_{ph} with ram pressure of $\dot{M}_{\text{B}} v_{\text{ff}}$. Therefore, the stability condition for super-Eddington accretion (i.e. $\dot{M}_{\text{B}} v_{\text{ff}} \gtrsim L/c$) is rewritten as

$$\frac{L}{L_{\text{Edd}}} \lesssim 83 \left(\frac{\dot{m}}{10^4} \right)^{5/6} \left(\frac{m_{\text{BH}}}{10^4} \right)^{1/6}. \quad (33)$$

As shown in Fig. 4, super-Eddington accretion for higher BH masses ($M_{\text{BH}} \gtrsim 10^2 M_{\odot}$) satisfy the stability condition after the transition occurs.

4.3 Cases with anisotropic radiation

We also examine cases with anisotropic disc radiation spectra. Under anisotropic radiation with a PL spectrum, hot ionized gas expands towards the bipolar directions, and the neutral warm gas with $T \simeq 8000 \text{ K}$ accretes through the equatorial plane at a rate of $\dot{M} \simeq \dot{M}_{\text{B}} \sin \Theta$ (Sugimura et al. 2017; Takeo et al. 2018), where Θ is the half angle of the neutral region measured from the equator. Moreover, the transition to efficient accretion where the entire region is covered by neutral gas occurs when $M_{\text{BH}} \times n_{\infty} \gtrsim 5 \times 10^{10} M_{\odot} \text{ cm}^{-3}$ is satisfied (Takeo et al. 2018). We mention how those features are affected by disc spectra in cases with/without transitions, respectively.

In cases without transitions, we compare a quantity of $\sin \Theta$ for the two cases. Fig. 9 presents two-dimensional distribution of the gas density (left-hand panels) and temperature (right-hand panels) under the disc spectrum (top) and the PL spectrum (bottom) for $M_{\text{BH}} \times n_{\infty} = 10^9 M_{\odot} \text{ cm}^{-3}$ and $\mathcal{N} = 4$ (hereafter Model 1e0M19N4; $\dot{M}_{\text{B}}/M_{\text{Edd}} = 7000$). The half angle for the disc spectrum ($\Theta_{\text{D}} \simeq 19^\circ$) at the Bondi radius becomes twice larger than

that for the PL spectrum ($\Theta_{\text{PL}} \simeq 10^\circ$). We can estimate the opening angle by solving $r_{\text{B}} = r_{\text{HII}}(\Theta)$, where

$$r_{\text{HII}}(\Theta) \approx \left[\frac{3(\mathcal{N} + 1)\dot{N}_{\text{ion}} \sin^{\mathcal{N}} \Theta}{4\pi n^2 \alpha_{\text{B}}} \right]^{1/3}, \quad (34)$$

and the angular dependence reflects the anisotropic radiation flux given in equation (20). Therefore, the ratio of the half-opening angle for the two cases is evaluated as

$$\frac{\sin \Theta_{\text{D}}}{\sin \Theta_{\text{PL}}} = \left(\frac{\dot{N}_{\text{ion,D}}}{\dot{N}_{\text{ion,PL}}} \right)^{-1/\mathcal{N}}. \quad (35)$$

For the disc spectrum, the ionizing photon number flux is given by

$$\dot{N}_{\text{ion,D}} \simeq \int_{v_{\text{tr}}}^{v_{\text{in}}} dv \frac{L_{\nu}^{\text{D,slim}}}{h\nu} \simeq 3.0 \times 10^{48} m_{\text{BH}}^{5/4} \text{ s}^{-1}, \quad (36)$$

where we approximately estimate $\dot{N}_{\text{ion,D}}$ taking account of the slim disc component because the accretion rate is as high as $\dot{m} \sim O(10^3)$. For a single PL spectrum, the photon flux is calculated as

$$\dot{N}_{\text{ion,PL}} = 4.90 \times 10^{48} m_{\text{BH}} \left[1 + \ln \left(\frac{\dot{m}}{20} \right) \right] \text{ s}^{-1}, \quad (37)$$

where the luminosity is estimated by equation (19). Therefore, we obtain the analytical expression of the ratio of the half-opening angles for $\mathcal{N} = 4$

$$\frac{\sin \Theta_{\text{D}}}{\sin \Theta_{\text{PL}}} \simeq 1.13 m_{\text{BH}}^{-1/16} \left[1 + \ln \left(\frac{\dot{m}}{20} \right) \right]^{1/4}. \quad (38)$$

This analytical expression agrees with the numerical results within errors of $\lesssim 10$ per cent.

In cases with the transition to the wholly neutral phase, the critical conditions can be derived by equating $r_{\text{HII}}/r_{\text{B}}$ at poles towards which

the radiation flux is collimated,

$$\frac{M_{\text{BH}} \times n_{\infty}}{10^9 M_{\odot} \text{ cm}^{-3}} \gtrsim \sqrt{\mathcal{N} + 1} \begin{cases} 7.1 [1 + \ln(\dot{m}/20)]^{1/2} & \text{(PL),} \\ 8.0 (m_{\text{BH}}/10)^{1/8} & \text{(Disc).} \end{cases} \quad (39)$$

We note that the criterion for $\mathcal{N} = 4$ agrees with the numerical result shown in Takeo et al. (2018).

4.4 Comparison with previous studies

Finally, we discuss the environmental conditions where the super-Eddington transition takes place. For stellar-mass BHs originated from gravitational collapse of massive Pop III stars, various negative feedback effects (stellar irradiation, energetic supernovae explosions, and BH radiation feedback) evacuate gas from shallow gravitational potential well of the host dark-matter halo and thus likely prevent the remnant BHs from accreting the ambient gas at super-Eddington rates (e.g. Kitayama et al. 2004; Kitayama & Yoshida 2005; Johnson, Greif & Bromm 2007; Alvarez et al. 2009). Even when a seed BH is embedded in a relatively massive halo, so-called atomic-cooling halo with a virial temperature of $\sim 10^4$ K, where gas would be tightly bound in the halo potential well, BH feedback and energetic supernovae would expel the gas at the vicinity of the BH and shut the BH growth off (e.g. Johnson et al. 2011; Dubois et al. 2012, 2015; Aykatalp et al. 2013; Prieto & Escala 2016; Latif, Volonteri & Wise 2018; Smidt et al. 2018). Although some studies mentioned above marginally resolve the Bondi radius for neutral warm gas with $T \sim 8000$ K, their prescriptions for energy and/or momentum feedback injected in unresolved regions still remain uncertain; namely, the density threshold above which the gas turns into stars is much smaller than the critical value for super-Eddington transitions for a heavy seed BH with $M_{\text{BH}} = 10^5 M_{\odot}$. Further studies using high-resolution cosmological simulations will be left in future. On the other hand, stellar-mass BHs embedded in the central gas-rich region of an atomic-cooling halo might grow at super-Eddington rates (e.g. Lupi et al. 2016; Ryu et al. 2016).

In this paper, we have explored several cases with different gas densities surrounding a BH. In reality, however, the boundary conditions would be set by external influences (e.g. rapid major mergers with other haloes) associated with cosmological large-scale structures. In the recent decade, large-scale cosmological simulations studying galaxy formation and evolution have been carried out intensively, e.g. FIRE (e.g. Hopkins et al. 2014), and Illustris (e.g. Vogelsberger et al. 2014) simulation. Some simulation studies (e.g. Di Matteo et al. 2017; Habouzit, Volonteri & Dubois 2017) focused on the early epoch of the Universe and investigated the relationships between growth of high- z BHs and the properties of their host haloes. As a sub-grid model to characterize rapid growth of BHs, the transition conditions would be applicable for those cosmological simulations which do not resolve the Bondi radius of the BHs.

5 SUMMARY AND CONCLUSIONS

We investigate the properties of accretion flows on to a BH with a mass of M_{BH} embedded in an initially uniform gas cloud with a density of n_{∞} in order to study rapid growth of BHs in the early Universe. In previous work, the conditions required for super-Eddington accretion from outside the Bondi radius were studied by assuming that radiation produced at the vicinity of the central BH has a single PL spectrum $\nu^{-\alpha}$ at $h\nu \geq 13.6$ eV ($\alpha \sim 1.5$). However, radiation spectra surely depends on the BH mass and accretion

rate, and determine the efficiency of radiative feedback. Here, we perform two-dimensional multifrequency radiation hydrodynamical simulations taking into account more realistic radiation spectra associated with the properties of nuclear accretion discs. We find that the critical density of gas surrounding the BH, above which a transition to super-Eddington accretion occurs, is alleviated for a wide range of masses of seed BHs ($10 \lesssim M_{\text{BH}}/M_{\odot} \lesssim 10^6$) because photoionization for accretion disc spectra are less efficient than those for single PL spectra with $1 \lesssim \alpha \lesssim 3$. For disc spectra, the transition to super-Eddington is more likely to occur for lower BH masses because the radiation spectra become too hard to ionize the gas. Even when accretion flows are exposed to anisotropic radiation, the effect due to radiation spectra shrinks the ionized region and likely leads to the transition to a wholly neutral accretion phase. Finally, by generalizing our simulation results, we construct a new analytical criterion required for super-Eddington accretion,

$$\left(\frac{M_{\text{BH}}}{10^5 M_{\odot}} \right) \left(\frac{n_{\infty}}{10^4 \text{ cm}^{-3}} \right) \gtrsim 2.4 \left(\frac{\langle \epsilon \rangle}{100 \text{ eV}} \right)^{-5/9}, \quad (40)$$

where $\langle \epsilon \rangle$ is the mean energy of ionizing radiation from the central BH.

ACKNOWLEDGEMENTS

We would like to thank Takaaki Kitaki for providing the spectral data of supercritical accretion flows. We also thank Daisuke Toyouchi for fruitful discussions. This work is partially supported by Japan Society for the Promotion of Science Grant-in-Aid for Scientific Research (A) (17H01102 KO), Scientific Research (C) (16K05309 KO; 18K03710 KO; 17K0583 SM), Scientific Research on Innovative Areas (18H04592 KO), and Young Scientists (17K14260 HRT), and supported by the National Key R&D Program of China (2016YFA0400702), and the National Science Foundation of China (11721303). This research is also supported by the Ministry of Education, Culture, Sports, Science and Technology of Japan as ‘Priority Issue on Post-K computer’ (Elucidation of the Fundamental Laws and Evolution of the Universe) and the Joint Institute for Computational Fundamental Science. Numerical computations were carried out on Cray XC30 and XC50 at Center for Computational Astrophysics, National Astronomical Observatory of Japan.

REFERENCES

- Abel T., Anninos P., Zhang Y., Norman M. L., 1997, *New Astron.*, 2, 181
 Abramowicz M. A., Czerny B., Lasota J. P., Szuszkiewicz E., 1988, *ApJ*, 332, 646
 Alexander T., Natarajan P., 2014a, *Science*, 345, 1330
 Alexander T., Natarajan P., 2014b, *Science*, 345, 1330
 Alvarez M. A., Wise J. H., Abel T., 2009, *ApJ*, 701, L133
 Aykatalp A., Wise J. H., Meijerink R., Spaans M., 2013, *ApJ*, 771, 50
 Bañados E. et al., 2018, *Nature*, 553, 473
 Begelman M. C., 1979, *MNRAS*, 187, 237
 Begelman M. C., Volonteri M., Rees M. J., 2006, *MNRAS*, 370, 289
 Bromm V., Loeb A., 2003, *ApJ*, 596, 34
 Chon S., Hirano S., Hosokawa T., Yoshida N., 2016, *ApJ*, 832, 134
 Ciotti L., Ostriker J. P., 2001, *ApJ*, 551, 131
 Ciotti L., Ostriker J. P., Proga D., 2009, *ApJ*, 699, 89
 Devecchi B., Volonteri M., 2009, *ApJ*, 694, 302
 Di Matteo T., Croft R. A. C., Feng Y., Waters D., Wilkins S., 2017, *MNRAS*, 467, 4243
 Done C., Kubota A., 2006, *MNRAS*, 371, 1216

- Draine B. T., 2011, *Physics of the Interstellar and Intergalactic Medium*, Princeton University Press, Princeton
- Dubois Y., Pichon C., Haehnelt M., Kimm T., Slyz A., Devriendt J., Pogosyan D., 2012, *MNRAS*, 423, 3616
- Dubois Y., Volonteri M., Silk J., Devriendt J., Slyz A., Teysseier R., 2015, *MNRAS*, 452, 1502
- Fabbiano G., Gioia I. M., Trinchieri G., 1989, *ApJ*, 347, 127
- Fan X. et al., 2004, *AJ*, 128, 515
- Glover S. C. O., Jappsen A.-K., 2007, *ApJ*, 666, 1
- Haardt F., Maraschi L., 1991, *ApJ*, 380, L51
- Habouzit M., Volonteri M., Dubois Y., 2017, *MNRAS*, 468, 3935
- Haiman Z., Loeb A., 2001, *ApJ*, 552, 459
- Harten A., Lax P. D., van Leer B., 1983, *SIAM Rev.*, 25, 35
- Hirano S., Hosokawa T., Yoshida N., Umeda H., Omukai K., Chiaki G., Yorke H. W., 2014, *ApJ*, 781, 60
- Hirano S., Hosokawa T., Yoshida N., Kuiper R., 2017, *Science*, 357, 1375
- Hopkins P. F., Kereš D., Oñorbe J., Faucher-Giguère C.-A., Quataert E., Murray N., Bullock J. S., 2014, *MNRAS*, 445, 581
- Hosokawa T., Omukai K., Yoshida N., Yorke H. W., 2011, *Science*, 334, 1250
- Hosokawa T., Omukai K., Yorke H. W., 2012, *ApJ*, 756, 93
- Hosokawa T., Yorke H. W., Inayoshi K., Omukai K., Yoshida N., 2013, *ApJ*, 778, 178
- Hosokawa T., Hirano S., Kuiper R., Yorke H. W., Omukai K., Yoshida N., 2016, *ApJ*, 824, 119
- Inayoshi K., Tanaka T. L., 2015, *MNRAS*, 450, 4350
- Inayoshi K., Omukai K., Tasker E., 2014, *MNRAS*, 445, L109
- Inayoshi K., Visbal E., Kashiyama K., 2015, *MNRAS*, 453, 1692
- Inayoshi K., Haiman Z., Ostriker J. P., 2016, *MNRAS*, 459, 3738
- Inayoshi K., Li M., Haiman Z., 2018, *MNRAS*, 479, 4017
- Jiang Y.-F., Stone J. M., Davis S. W., 2014, *ApJ*, 796, 106
- Johnson J. L., Greif T. H., Bromm V., 2007, *ApJ*, 665, 85
- Johnson J. L., Khochfar S., Greif T. H., Durier F., 2011, *MNRAS*, 410, 919
- Kato Y., Mineshige S., Shibata K., 2004, *ApJ*, 605, 307
- Kato S., Fukue J., Mineshige S., 2008, *Black-Hole Accretion Disks – Towards a New Paradigm*, Kyoto University Press, Kyoto
- Katz H., Sijacki D., Haehnelt M. G., 2015, *MNRAS*, 451, 2352
- Kawashima T., Ohsuga K., Mineshige S., Heinzeller D., Takabe H., Matsumoto R., 2009, *PASJ*, 61, 769
- Kawashima T., Ohsuga K., Mineshige S., Yoshida T., Heinzeller D., Matsumoto R., 2012, *ApJ*, 752, 18
- King A., 2003, *ApJ*, 596, L27
- King A. R., Davies M. B., Ward M. J., Fabbiano G., Elvis M., 2001, *ApJ*, 552, L109
- Kitaki T., Mineshige S., Ohsuga K., Kawashima T., 2017, *PASJ*, 69, 92
- Kitaki T., Mineshige S., Ohsuga K., Kawashima T., 2018, *PASJ*, 70, 108
- Kitayama T., Yoshida N., 2005, *ApJ*, 630, 675
- Kitayama T., Yoshida N., Susa H., Umemura M., 2004, *ApJ*, 613, 631
- Kormendy J., Ho L. C., 2013, *ARA&A*, 51, 511
- Latif M. A., Volonteri M., Wise J. H., 2018, *MNRAS*, 476, 5016
- Li Y. et al., 2007, *ApJ*, 665, 187
- Liu B. F., Mineshige S., Shibata K., 2002, *ApJ*, 572, L173
- Liu B. F., Mineshige S., Ohsuga K., 2003, *ApJ*, 587, 571
- Loeb A., Rasio F. A., 1994, *ApJ*, 432, 52
- Lupi A., Haardt F., Dotti M., Fiacconi D., Mayer L., Madau P., 2016, *MNRAS*, 456, 2993
- Madau P., Rees M. J., 2001, *ApJ*, 551, L27
- Madau P., Haardt F., Dotti M., 2014, *ApJ*, 784, L38
- Meyer F., Meyer-Hofmeister E., 1981, *A&A*, 104, L10
- Milosavljević M., Couch S. M., Bromm V., 2009a, *ApJ*, 696, L146
- Milosavljević M., Bromm V., Couch S. M., Oh S. P., 2009b, *ApJ*, 698, 766
- Mineshige S., Hirano A., Kitamoto S., Yamada T. T., Fukue J., 1994, *ApJ*, 426, 308
- Mineshige S., Kawaguchi T., Takeuchi M., Hayashida K., 2000, *PASJ*, 52, 499
- Mortlock D. J. et al., 2011, *Nature*, 474, 616
- Murray N., Quataert E., Thompson T. A., 2005, *ApJ*, 618, 569
- Narayan R., Sądowski A., Soria R., 2017, *MNRAS*, 469, 2997
- Ohsuga K., Mineshige S., 2007, *ApJ*, 670, 1283
- Ohsuga K., Mineshige S., 2011, *ApJ*, 736, 2
- Ohsuga K., Mori M., Nakamoto T., Mineshige S., 2005, *ApJ*, 628, 368
- Ohsuga K., Mineshige S., Mori M., Kato Y., 2009, *PASJ*, 61, L7
- Oh S. P., Haiman Z., 2002, *ApJ*, 569, 558
- Omukai K., Schneider R., Haiman Z., 2008, *ApJ*, 686, 801
- Pacucci F., Ferrara A., 2015, *MNRAS*, 448, 104
- Park K., Ricotti M., 2011, *ApJ*, 739, 2
- Park K., Ricotti M., 2012, *ApJ*, 747, 9
- Pezzulli E., Valiante R., Schneider R., 2016, *MNRAS*, 458, 3047
- Pezzulli E., Volonteri M., Schneider R., Valiante R., 2017, *MNRAS*, 471, 589
- Prieto J., Escala A., 2016, *MNRAS*, 460, 4018
- Regan J. A., Haehnelt M. G., 2009a, *MNRAS*, 393, 858
- Regan J. A., Haehnelt M. G., 2009b, *MNRAS*, 396, 343
- Regan J. A., Johansson P. H., Wise J. H., 2016a, *MNRAS*, 459, 3377
- Regan J. A., Johansson P. H., Wise J. H., 2016b, *MNRAS*, 461, 111
- Reinoso B., Schleicher D. R. G., Fellhauer M., Klessen R. S., Boekholt T. C. N., 2018, *A&A*, 614, A14
- Ricotti M., Gnedin N. Y., Shull J. M., 2002, *ApJ*, 575, 33
- Ryu T., Tanaka T. L., Perna R., Haiman Z., 2016, *MNRAS*, 460, 4122
- Sakurai Y., Inayoshi K., Haiman Z., 2016, *MNRAS*, 461, 4496
- Sakurai Y., Yoshida N., Fujii M. S., Hirano S., 2017, *MNRAS*, 472, 1677
- Shakura N. I., Sunyaev R. A., 1973, *A&A*, 24, 337
- Shull J. M., 1979, *ApJ*, 234, 761
- Shull J. M., van Steenberg M. E., 1985, *ApJ*, 298, 268
- Silk J., Rees M. J., 1998, *A&A*, 331, L1
- Smidt J., Whalen D. J., Johnson J. L., Surace M., Li H., 2018, *ApJ*, 865, 126
- Soltan A., 1982, *MNRAS*, 200, 115
- Stacy A., Greif T. H., Bromm V., 2012, *MNRAS*, 422, 290
- Stone N. C., Küpper A. H. W., Ostriker J. P., 2017, *MNRAS*, 467, 4180
- Sugimura K., Hosokawa T., Yajima H., Omukai K., 2017, *MNRAS*, 469, 62
- Sugimura K., Hosokawa T., Yajima H., Inayoshi K., Omukai K., 2018, *MNRAS*, 478, 3961
- Svensson R., Zdziarski A. A., 1994, *ApJ*, 436, 599
- Sądowski A., Narayan R., Tchekhovskoy A., Abarca D., Zhu Y., McKinney J. C., 2015, *MNRAS*, 447, 49
- Takahashi H. R., Ohsuga K., 2013, *ApJ*, 772, 127
- Takahashi H. R., Ohsuga K., Kawashima T., Sekiguchi Y., 2016, *ApJ*, 826, 23
- Takeo E., Inayoshi K., Ohsuga K., Takahashi H. R., Mineshige S., 2018, *MNRAS*, 476, 673
- Tanaka T., Haiman Z., 2009, *ApJ*, 696, 1798
- Toyouchi D., Hosokawa T., Sugimura K., Nakatani R., Kuiper R., 2019, *MNRAS*, 483, 2031
- Valiante R., Schneider R., Volonteri M., Omukai K., 2016, *MNRAS*, 457, 3356
- Valiante R., Schneider R., Graziani L., Zappacosta L., 2018, *MNRAS*, 474, 3825
- van Leer B., 1977, *J. Comput. Phys.*, 23, 263
- Visbal E., Haiman Z., Bryan G. L., 2014, *MNRAS*, 445, 1056
- Vogelsberger M. et al., 2014, *Nature*, 509, 177
- Volonteri M., Rees M. J., 2005, *ApJ*, 633, 624
- Volonteri M., Haardt F., Madau P., 2003, *ApJ*, 582, 559
- Wang J.-M., Szuszkiewicz E., Lu F.-J., Zhou Y.-Y., 1999, *ApJ*, 522, 839
- Watarai K.-y., 2006, *ApJ*, 648, 523
- Watarai K.-y., Fukue J., Takeuchi M., Mineshige S., 2000, *PASJ*, 52, 133
- Watarai K.-y., Mizuno T., Mineshige S., 2001, *ApJ*, 549, L77
- Whalen D., Norman M. L., 2006, *ApJS*, 162, 281
- Wu X.-B. et al., 2015, *Nature*, 518, 512
- Yajima H., Khochfar S., 2016, *MNRAS*, 457, 2423
- Yoshida N., Omukai K., Hernquist L., 2008, *Science*, 321, 669
- Yu Q., Tremaine S., 2002, *MNRAS*, 335, 965

This paper has been typeset from a $\text{\TeX}/\text{\LaTeX}$ file prepared by the author.